



Characterization of $\text{SrCo}_{0.7}\text{Fe}_{0.2}\text{Nb}_{0.1}\text{O}_{3-\delta}$ cathode materials for intermediate-temperature solid oxide fuel cells



Shiquan Lü ^{a,b}, Bo Yu ^a, Xiangwei Meng ^{a,b}, Xiaoyu Zhao ^a, Yuan Ji ^b, Chengwei Fu ^b, Yongjun Zhang ^a, Lili Yang ^a, Hougang Fan ^a, Jinghai Yang ^{a,*}

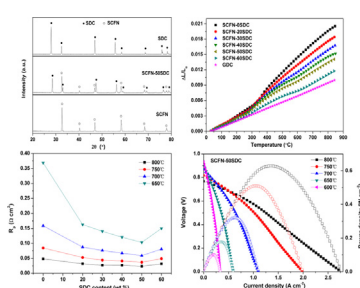
^a Key Laboratory of Functional Materials Physics and Chemistry of the Ministry of Education, Jilin Normal University, Siping 136000, PR China

^b State Key Laboratory of Superhard Materials, Jilin University, Changchun 130051, PR China

HIGHLIGHTS

- A cubic structure $\text{SrCo}_{0.7}\text{Fe}_{0.2}\text{Nb}_{0.1}\text{O}_{3-\delta}$ (SCFN) cathode is prepared by a solid state reaction.
- The electrical conductivity of the SCFN sample reaches a maximum 304 S cm^{-1} at 350°C in air.
- The thermal expansion coefficients of SCFN cathode decrease greatly with SDC addition.
- The addition of SDC to SCFN cathode reduces the polarization resistance.
- High power density of 630 mW cm^{-2} at 800°C for SCFN–50SDC is obtained on SDC electrolyte.

GRAPHICAL ABSTRACT



ARTICLE INFO

Article history:

Received 31 May 2014

Received in revised form

19 August 2014

Accepted 15 September 2014

Available online 22 September 2014

Keywords:

Solid oxide fuel cell

Cathode

$\text{SrCo}_{0.7}\text{Fe}_{0.2}\text{Nb}_{0.1}\text{O}_{3-\delta}$

Electrochemical performance

ABSTRACT

A new cubic perovskite oxide, $\text{SrCo}_{0.7}\text{Fe}_{0.2}\text{Nb}_{0.1}\text{O}_{3-\delta}$ (SCFN), is investigated as a cathode for intermediate-temperature solid oxide fuel cells (IT-SOFCs). XRD results show that there are no serious reactions between SCFN and $\text{Sm}_{0.2}\text{Ce}_{0.8}\text{O}_{1.9}$ (SDC) except a slight peak shift. XPS analysis shows that the transition-metal cations in the SCFN exist in two different valence states, i.e., $[\text{Sr}^{2+}][\text{Co}^{3+}/\text{Co}^{4+}]_{0.7}[\text{Fe}^{3+}/\text{Fe}^{4+}]_{0.2}[\text{Nb}^{4+}/\text{Nb}^{5+}]_{0.1}\text{O}_{3-\delta}$. The electrical conductivity of the SCFN sample reaches a maximum 304 S cm^{-1} at 350°C in air. In order to optimize thermal expansion coefficients (TECs) and electrochemical performance of the SCFN cathode, we fabricate SCFN-xSDC ($x = 0, 20, 30, 40, 50, 60$, wt%) composite cathodes. The thermal expansion behavior shows that the TECs value of SCFN cathode decreases greatly with SDC addition. The SDC addition reduces the polarization resistance, and the lowest polarization resistance $0.0255 \Omega \text{ cm}^2$ is achieved at 800°C for SCFN–50SDC composite cathode. For SCFN-xSDC ($x = 0, 40, 50, 60$) composites, the maximum power densities of single-cells with SCFN-xSDC cathodes on $300 \mu\text{m}$ thick SDC electrolyte achieve $417, 557, 630$ and 517 mW cm^{-2} at 800°C , respectively. These results indicate that SCFN–50SDC composite is a potential cathode material for application in IT-SOFCs.

© 2014 Elsevier B.V. All rights reserved.

1. Introduction

Lowering the operating temperature of solid oxide fuel cells (SOFCs) to the intermediate-temperature (IT, 500 – 800°C) is one of the main goals in current SOFCs research [1,2]. However, a key

* Corresponding author. Tel./fax: +86 434 3294566.

E-mail address: jhyang@jlnu.edu.cn (J. Yang).

obstacle to develop IT-SOFCs is the large cathode polarization resistance caused by the reduced temperature. And one effective way is to develop the new mixed ionic-electronic conducting (MIEC) cathode materials. Most studies of MIEC cathodes focus on perovskites, such as doped LaCoO₃, BaCoO₃ or LaFeO₃ [3–7].

The MIEC oxide SrCoO_{3-δ} is a very important compound that can be further developed into many functional materials such as oxygen separation membranes, combustion catalysts and SOFC cathodes [8–14]. The structural evolution research showed that the phase structure and electrical conductivity of SrCoO_{3-δ} was closely related with the oxygen content in the composite, which could take a wide range of variation [11,15]. Among the various phase structures of SrCoO_{3-δ}, the oxide with the cubic phase exhibits the highest electrical conductivity and oxygen permeability values. Deng et al. reported that the electrical conductivity of cubic phase SrCoO_{3-δ} was 210 S cm⁻¹ at 830 °C [16]. And the cubic phase SrCoO_{3-δ} exhibits markedly large oxide ion conductivity (2.5 S cm⁻¹ at 900 °C), which is several orders of magnitude higher than the typical high oxygen ionic conducting electrolyte of samaria-doped ceria. However, cobalt-rich compositions often show high thermal expansion coefficients (TECs) [17,18]. Some studies have shown that the partial substitution of Co by Fe could reduce the TECs of cobalt-based materials by the decrease in Co content and depressing the spin-state transition of the cobalt ions from low spin to high spin [19]. However, the SrCo_{0.8}Fe_{0.2}O_{3-δ} oxide undergoes phase transition from cubic perovskite to brownmillerite structure when it is heated in air [20,21]. The brownmillerite structure has low ionic conductivity due to its oxygen vacancy ordering and shows almost non-oxygen permeable properties at lower temperatures, which limits its practical applications in oxygen separation devices and SOFCs [21]. Recently, Nagai et al. [22] demonstrated the Nb is the most effective dopant in SrCoO_{3-δ}-based oxide for improving the phase stability and oxygen permeability. More recently, Podyacheva et al. [23] systematically investigated the properties of SrCo_{0.8-x}Fe_{0.2}Nb_xO_{3-δ} ($x = 0.1\text{--}0.3$) perovskites in oxidizing and reducing environments. Their results indicate that the Nb doping content has a significant effect on the phase structure stability of the SrCo_{0.8}Fe_{0.2}O_{3-δ} oxides, and thus significantly extends the application scopes of the SrCo_{0.8-x}Fe_{0.2}Nb_xO_{3-δ} materials. This would also lead to interesting possibilities in terms of developing cathode materials for IT-SOFCs. Meanwhile, it is widely accepted that composite cathodes show some improved electrochemical properties. For example, compared

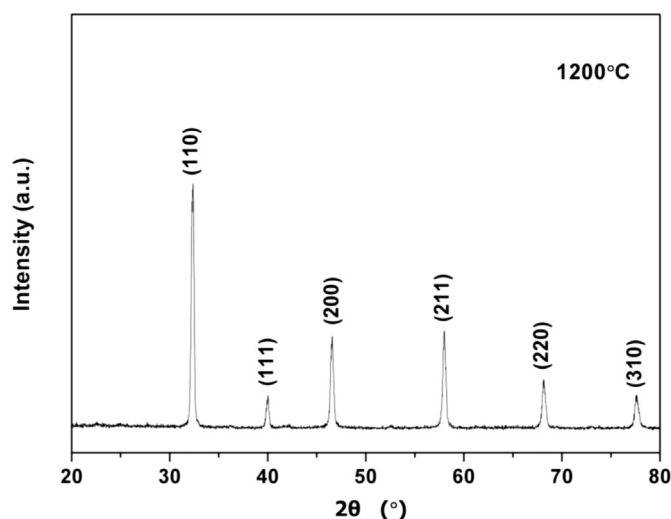


Fig. 1. XRD pattern of SCFN sintered at 1200 °C for 12 h.

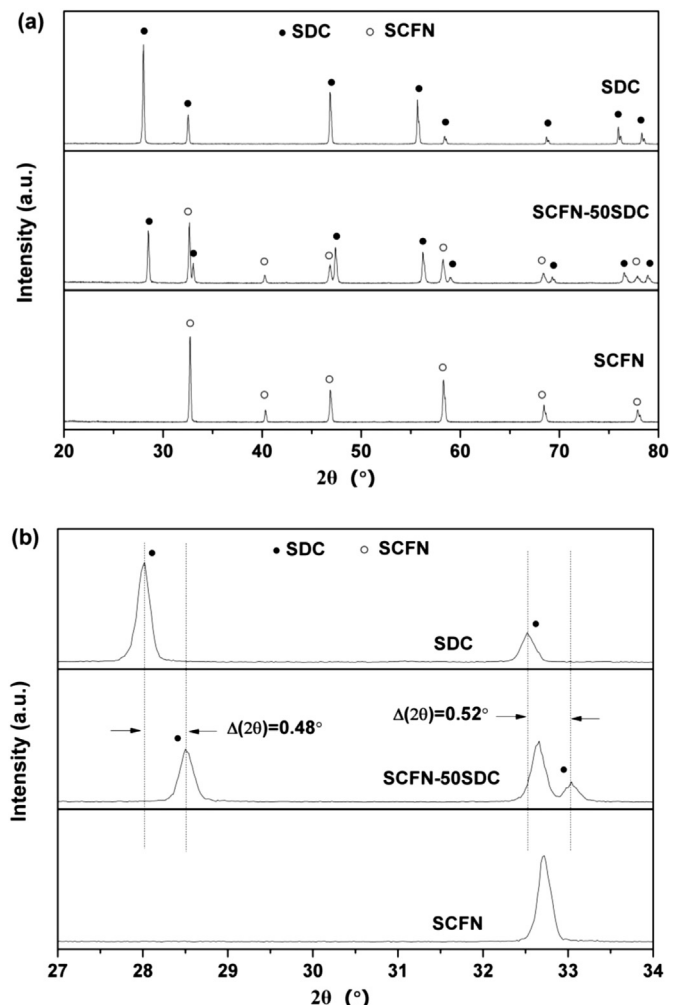


Fig. 2. (a) XRD patterns for sintered SCFN, SCFN–50SDC and SDC powders; (b) magnified XRD patterns from 27° to 34°.

to (La,Sr)(Co,Fe)O₃, the composites consisting of (La,Sr)(Co,Fe)O₃ and Ce_{0.9}Gd_{0.1}O_{1.95} show the low interfacial polarization resistances over a temperature range of 500–700 °C, because the composite cathodes expand the active triple-phase boundaries (TPBs) from

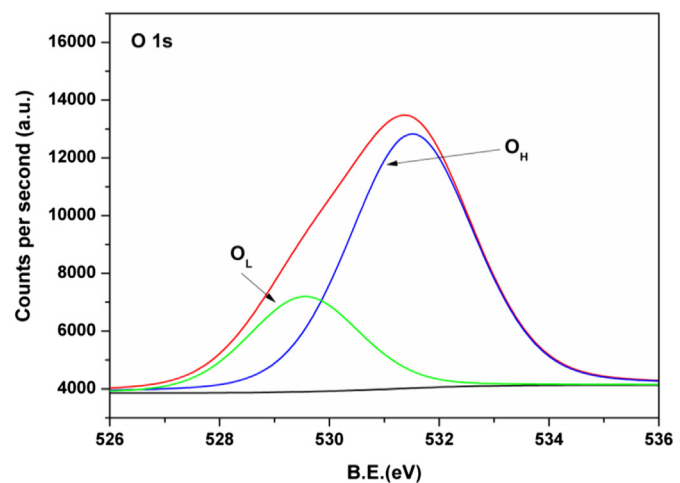


Fig. 3. XPS spectra of O 1s in the SCFN sample at room temperature.

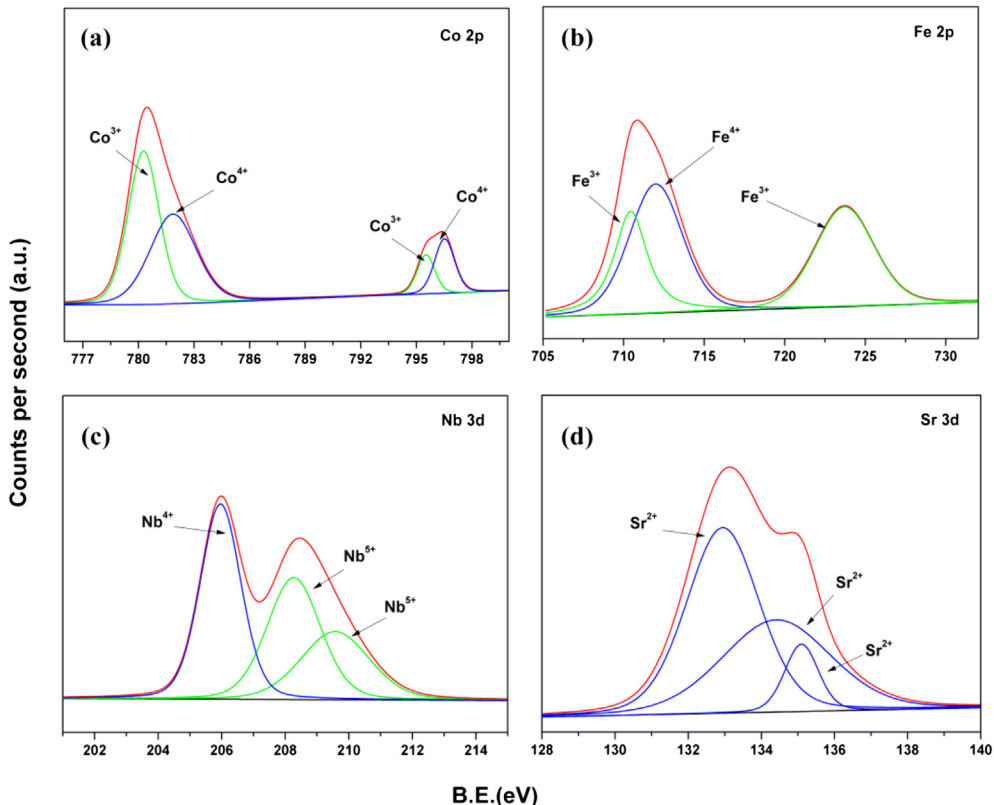


Fig. 4. XPS spectra at room temperature for the SCFN sample: (a) Co 2p, (b) Fe 2p, (c) Nb 3d and (d) Sr 3d.

the two-dimensional interface between the electrolyte and the cathode to the entire zone of the cathode [24–26]. In addition, the composite cathodes have a decreased TEC which matches to IT-SOFCs electrolyte materials.

In this study, we fabricate SCFN cubic perovskite oxide as a cathode material and analyze its chemical compatibility with SDC electrolyte. Subsequently, the composite cathodes SCFN-xSDC ($x = 0, 20, 30, 40, 50, 60$, wt%) are prepared, and the effects of SDC content are investigated under IT-SOFCs operating conditions.

2. Experimental

2.1. Powder synthesis and cell fabrication

The samples of $\text{SrCo}_{0.7}\text{Fe}_{0.2}\text{Nb}_{0.1}\text{O}_{3-\delta}$ (SCFN) were synthesized by a solid state reaction. Stoichiometric amounts of commercial powders SrCO_3 (99%), Nb_2O_5 (99%), Fe_2O_3 (99%) and Co_3O_4 (99%) were weighed and mixed according to the composition of SCFN. The mixed powders were ground thoroughly with ethanol as grinding medium using an agate pestle and mortar. The obtained precursors were pressed into pellets and calcined repeatedly at 1000, 1100 and 1200 °C for 12 h in air with intermediate grindings, respectively. Powders of SDC were synthesized using the glycine-nitrate combustion method [27]. The composite materials SCFN-xSDC were prepared by incorporating SDC into SCFN, milled with an agate mortar for 2 h. The samples added with SDC (0, 20, 30, 40, 50 and 60, wt%) were noted as SCFN-xSDC ($x = 0, 20, 30, 40, 50$ and 60, wt%). Suitable slurries were made by mixing SCFN-xSDC powders with an appropriate organic solvent (10% ethyl cellulose + 90% terpineol). Then, the cathode slurry was painted onto both surfaces of the SDC pellet in symmetric configuration and subsequently calcinated at 950 °C for 2 h under an air atmosphere. The performance of SCFN

cathode was evaluated in an electrolyte-supported fuel cell. Ni + SDC mixture was used as the anode and SDC was used as the electrolyte with a thickness of 300 μm . The anode was painted on one side of the SDC pellet and sintered at 1250 °C for 4 h in air. The SCFN-xSDC slurry was painted on the other side of the SDC electrolyte and then sintered at 950 °C for 2 h in air. The single-cell was sealed on one end of an alumina tube with silver paste.

2.2. Electrochemical characterization

The performance of the single-cell was measured using an electrochemical workstation (CHI 660C, Chenhua Inc., Shanghai).

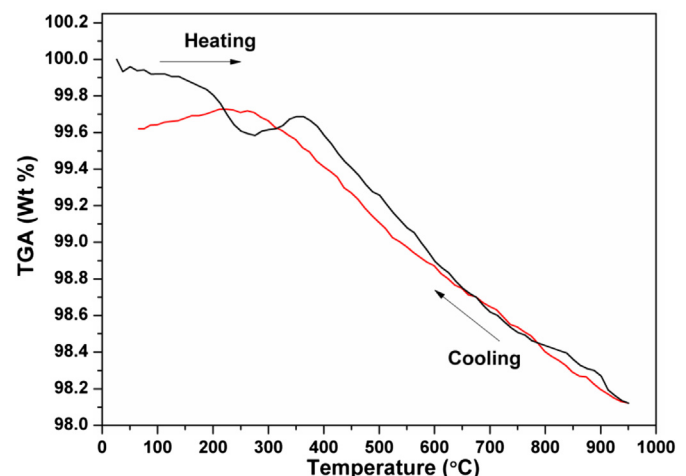


Fig. 5. TGA curve of the SCFN sample in the temperature range of 30–950 °C in air.

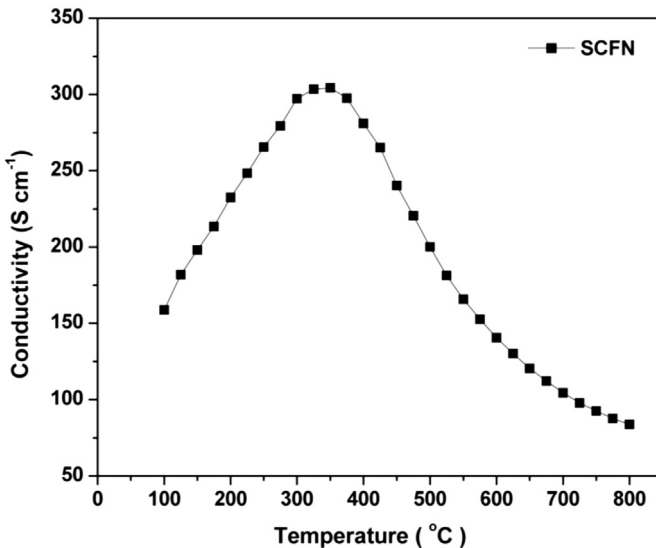


Fig. 6. Temperature dependence of the conductivity for SCFN sample.

H_2 fuel was fed into the anode chamber at a flow rate of 100 ml min⁻¹, and ambient air served as the oxidant gas. The electrochemical impedance spectra of the cathode were investigated using the same electrochemical system. The applied frequency range was from 0.01 Hz to 100 kHz and the signal amplitude was 10 mV under open cell voltage (OCV) conditions. A measurement temperature range of 600–800 °C was adopted in increments of 50 °C for all the samples.

2.3. Other characterization

The phase composition of the synthesized powders and the phase reaction between cathode and electrolyte were identified using an X-ray diffractometer (XRD) (Rigaku-D-Max γA). The scans were performed in the 2θ range of 20–80° with an angle step of 0.02°, at room temperature. A thermogravimetric analysis (TGA) curve was obtained using a thermal analyzer (HENVEN HCT-3) in air at a rate of 50 ml min⁻¹. The sample was measured between 30 and 950 °C with

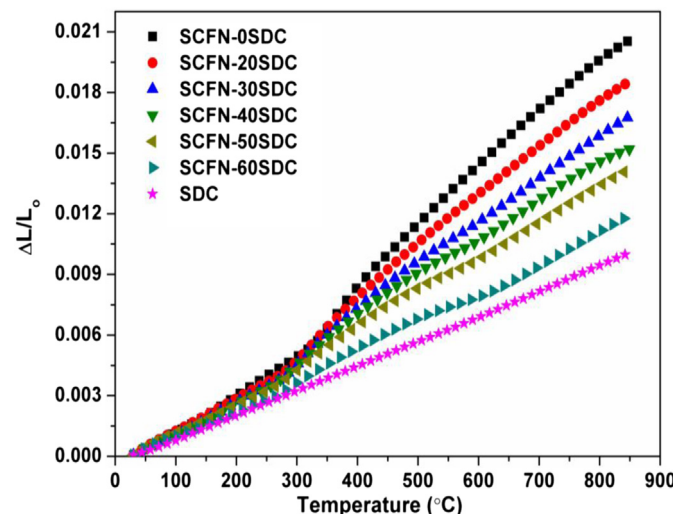


Fig. 7. Thermal expansion curves of the SCFN-xSDC composite cathodes and SDC electrolyte between 30 and 850 °C in air.

a heating/cooling rate of 5 °C min⁻¹. The electrical conductivity was measured by the Van der Pauw method. In this measurement, the SCFN powder was dry-pressed into pellets about 13 mm in diameter and 0.63 mm thick under 200 MPa, and sintered at 950 °C for 2 h to obtain a dense cathode substrate. The density was about 89.7% as determined using Archimedes water displacement method. Ag paste was used for the electrodes and placed at the circumference of the sample. The thermal expansion coefficients were measured with cylindrical samples, about 6 mm (diameter) × 4.9 mm (height). The cylinders were prepared by pressing SCFN-xSDC powders at 200 MPa and sintering at 950 °C for 2 h. And the density of the SCFN-xSDC cylindrical samples was about 86.4–88.9%. The thermal expansion coefficients were measured using a horizontal dilatometer (Netzsch DIL 402C) over a temperature range of 30–850 °C in air with a flowing rate of 60 ml min⁻¹, and a heating rate of 5 °C min⁻¹. Scanning electron microscope (SEM) studies were performed using a JEOL JSM-6480LV microscope equipped with an EDAX CDU Detection system for the EDS analysis.

3. Results and discussion

3.1. XRD and chemical compatibility

Fig. 1 shows the room-temperature XRD pattern of SCFN sample sintered at 1200 °C for 12 h in air through intermediate grinding and calcining at 1000 and 1100 °C. The pattern of pure SCFN exhibits pure phase and high crystallinity, and no peaks of any impurities are observed. The diffraction peaks of SCFN can be indexed based on the PDF card no. 82-2445, with a cubic perovskite structure. The unit-cell parameters are calculated from the XRD patterns. For a cubic structure, the unit-cell parameters of SCFN are as follows: $a = 0.389347$ nm and cell volume $V = 0.059022$ nm³. The interfacial reaction between electrode and electrolyte is highly deleterious, which increases the interfacial polarization resistances, and results in the degradation of the SOFCs performance [28]. To examine the chemical compatibility between electrode and electrolyte, XRD is used to detect the phase reaction of the SCFN cathode with SDC electrolyte. Fig. 2(a) shows an XRD pattern of the SCFN-50SDC composite cathode. For comparison, the patterns of SDC and SCFN are also shown in the same figure. After sintered at 950 °C for 5 h, all the diffraction peaks could be indexed well based on a physical mixture of SCFN and SDC phases, which indicates that no serious reaction is detected in the binary-mixed SCFN-50SDC

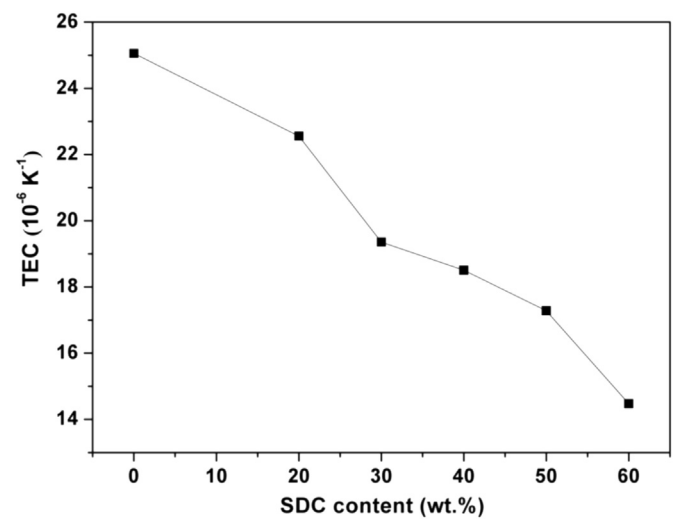


Fig. 8. Dependence of TEC for SCFN-xSDC cathodes with different SDC content.

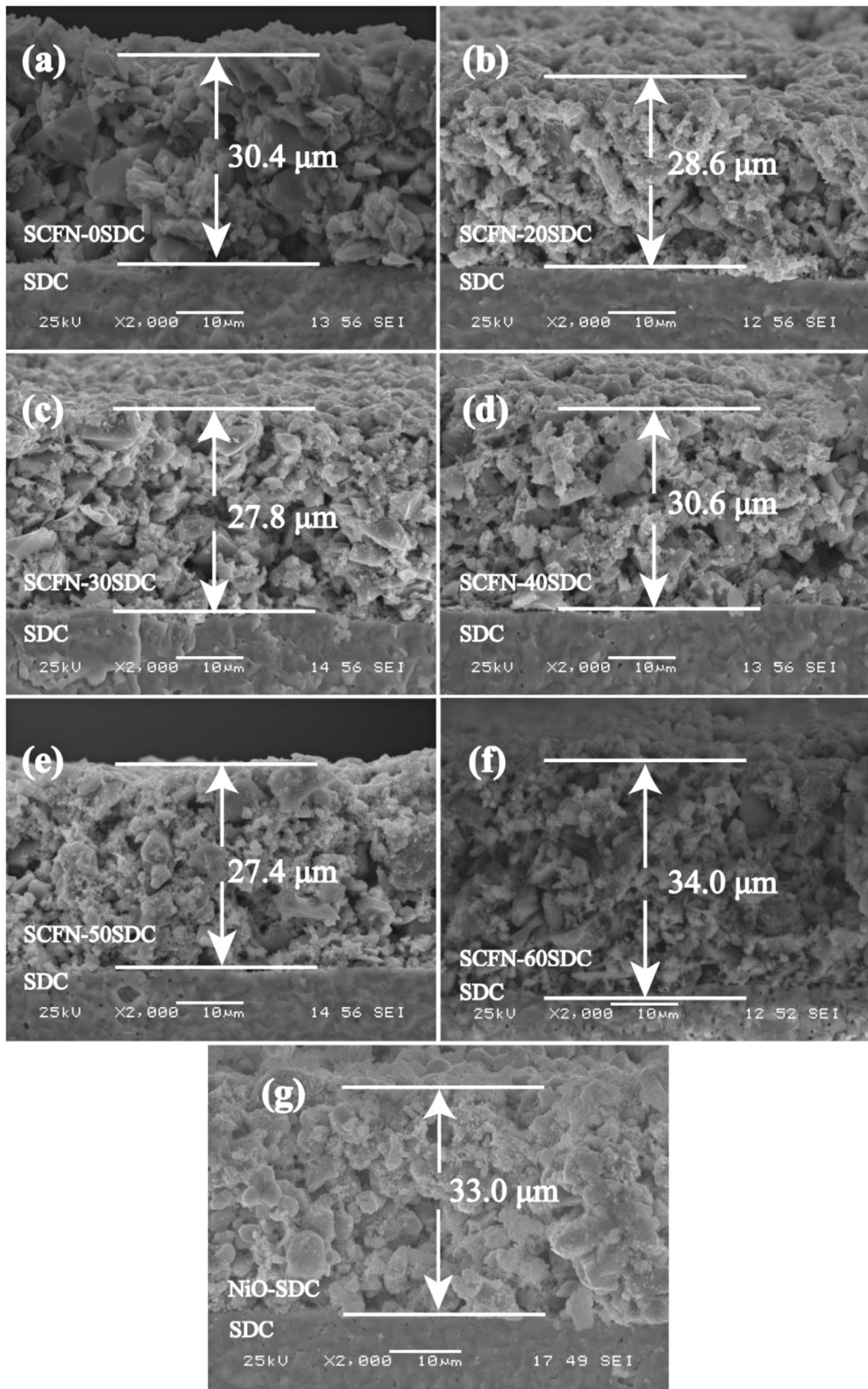


Fig. 9. Cross-sectional SEM micrographs of SCFN- x SDC cathodes and NiO-SDC anode on SDC electrolyte.

systems upon sintering at 950 °C for 5 h. However, the main peaks for SDC in the SCFN–50SDC shift obviously to the high angle direction indicating the shrinking of lattice parameter, which can be seen clearly in the magnified XRD pattern for the Bragg angle range of $27^\circ \leq 2\theta \leq 34^\circ$ (Fig. 2(b)). The peak shifts of the SDC are probably due to the diffusion of the Sm³⁺ ion from SDC to SCFN since the lattice constant of Sm doped ceria is larger than that of undoped ceria [29]. Li et al. have reported that diffusion of Sm from SDC into Ba_{0.5}Sr_{0.5}Co_{0.6}Fe_{0.4}O_{3-δ} is possible [30].

3.2. XPS analysis

The XPS spectra are used to characterize the element chemical environment. The chemical environments of O, Co, Fe, Nb and Sr ions are estimated by curve-fitting of the O 1s, Co 2p, Fe 2p, Nb 3d and Sr 3d spectra, as shown in Figs. 3 and 4. In Fig. 3, the O 1s core-level spectrum consists of two components at 529.1 and 531.4 eV. The former is a typical feature of hydroxyl group and carbonate structure (O_H), and the latter comes from the oxygen lattice (O_L) [31]. Fig. 4(a) shows the Co 2p core-level spectra of the SCFN sample. The main peaks located at 781.9 and 796.5 eV are obviously distinguishable from each other, representing Co⁴⁺ 2p_{3/2} and Co⁴⁺ 2p_{1/2}. The binding energies at 780.2 and 795.5 eV are considered as features of Co³⁺ 2p_{3/2} and Co³⁺ 2p_{1/2} [32,33]. No high binding energy satellites at 785.0–788.0 eV are observed in the Co 2p core-level XPS spectra, indicating the absence of Co²⁺ species [34]. The mixture valence of Co³⁺ and Co⁴⁺ exists in the SCFN sample. In Fig. 4(b), the Fe³⁺ (2p_{3/2}) and Fe³⁺ (2p_{1/2}) peaks are observed at 710.4 eV and 723.7 eV respectively, whereas Fe⁴⁺ (2p_{3/2}) shows a peak at 712.0 eV. The XPS data reveals iron as having Fe^{3+}/Fe⁴⁺ mixed chemical states for the SCFN sample. Similar phenomenon was also observed by Jung et al. in perovskite oxide Ba_{0.5}Sr_{0.5}Co_xFe_{1-x}O_{3-δ} [35]. Fig. 4(c) shows the Nb 3d core-level XPS spectra of the SCFN sample. The characteristic peaks of Nb⁴⁺ and Nb⁵⁺ are 206.0 eV at 3d_{5/2} and 208.3 and 209.5 eV at 3d_{3/2}. Similar results have been previously observed [36], indicating that the oxidation states of Nb in the compound are 4+ and 5+. The Sr 3d core-level XPS spectrum of the SCFN sample is shown in Fig. 4(d). Only one chemical state of strontium is found in the sample, indicating that the contribution to the spectra of pure Sr–O structure originates from cubic-perovskite SCFN as well as minor strontium carbonate and hydroxyl groups. The XPS results clearly indicate the existence of Fe^{3+}/Fe⁴⁺, Co^{3+}/Co⁴⁺, Nb^{4+}/Nb⁵⁺, and Sr²⁺ species in the SCFN sample.}}}}

3.3. TGA and electrical conductivity

In order to study the thermal stability of the SCFN sample, TGA measurement is performed in air between 30 and 950 °C during heating and cooling processes. Fig. 5 presents the TGA curve for the SCFN sample. A small mass loss is observed in the curve before 200 °C, which is associated with desorption of moisture, carbon dioxide, and oxygen. A significant linear weight loss from 350 °C should correspond to the loss of lattice oxygen in the SCFN sample.

In SCFN mixed conductors, the total electrical conductivity involves the electronic and the oxygen ionic conductivity. The oxygen ionic conductivity is clearly lower than the electronic conductivity. Therefore the measured conductivity values can be mainly considered as the electronic conductivity. Fig. 6 shows the electrical conductivity behaviors of SCFN sample measured in air. The electrical conductivity increases with the increasing temperature, which presents a semiconductor-like behavior and reaches a maximum value 304 S cm⁻¹ at 350 °C. Thereafter, the electrical conductivity decreases gradually, which is characteristic of metallic-like behavior. This result shows the SCFN oxide undergoes

a change from the semiconductor-like conduction behavior to the metal-like around 350 °C. Similar observations are also reported for cobalt-based perovskite oxides [13,37]. In the SCFN system, the donor doping of Nb^{5+}/Nb⁴⁺ at the B site may result in the partial reduction of (Co, Fe)⁴⁺ to (Co, Fe)³⁺ as electronic charge compensation, which is confirmed by the XPS results. Therefore, the semiconductor-to-metal transition in SCFN cathode can be mainly attributed to the reduction of (Co, Fe)⁴⁺ to (Co, Fe)³⁺, accompanied by the loss of lattice oxygen and the formation of oxygen vacancies [13,38]. This result is in agreement with the TGA observation in Fig. 5. Below 350 °C, the semiconductor-like behavior of SCFN sample is attributed to the hopping conduction mechanism of the small polarons through the transport of the electron holes [39]. The charge compensation for SCFN is primarily electrons at low temperatures, and the conductivity can be attributed to the migration of electron holes. Above 350 °C, the ionic compensation is dominantly due to the loss of the lattice oxygen, leading to a decrease in the oxygen content of the SCFN. According to the defect reaction written in the Kröger–Vink notation.}



$$e' + h^{\bullet} = 0 \quad (2)$$

The increased concentration of oxygen vacancies decreases the concentration of electron holes. Therefore, the electrical conductivity decreases to show metallic-like behavior above 350 °C [37,39]. Nevertheless, the conductivity values of the SCFN sample are 83–200 S cm⁻¹ within the operating temperature range of IT-SOFCs, which is much higher than other SrCoO_{3-δ} and BaCoO_{3-δ}-based oxides. For example, the maximum values are 50 and 13 S cm⁻¹ for Ba_{0.5}Sr_{0.5}Co_{0.8}Fe_{0.2}O_{3-δ} [40] and BaCo_{0.7}Fe_{0.2}Nb_{0.1}O_{3-δ} [41], respectively. Therefore, it is feasible to use SCFN oxide as a cathode material in IT-SOFCs.

3.4. Thermal expansion

In the fuel cells, the TECs of the electrode and electrolyte should be taken into account because the mismatch of TECs will result in the thermal stresses, residual stresses, and the following degradation of the fuel cells [42]. In this experiment, SDC is introduced to

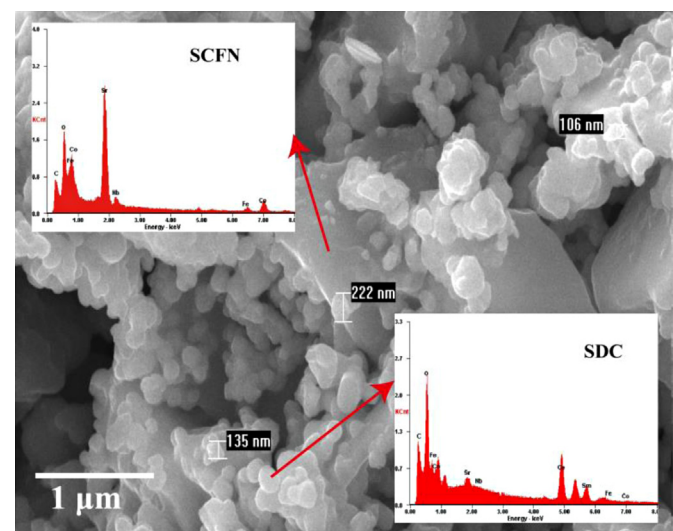


Fig. 10. Surface microstructure and EDS results of the SCFN–50SDC composite structure.

match the TECs between SCFN and SDC. The thermal expansion behavior of the SDC and SCFN-xSDC is measured in air (Fig. 7), and Fig. 8 shows the average TEC values between 30 and 850 °C as a function of SDC proportion in SCFN. Pure SCFN possesses a high value of TEC ($25.06 \times 10^{-6} \text{ K}^{-1}$), while the TEC of SDC is $12.39 \times 10^{-6} \text{ K}^{-1}$. And this mismatch of TECs will inevitably impair the longevity of SOFCs. As expected, the introduction of SDC into SCFN efficiently reduces the TEC of the composite cathodes and decreases the mechanical mismatch between cathode and electrolyte materials. For instance, the TEC value of SCFN-60SDC is equal to $13.53 \times 10^{-6} \text{ K}^{-1}$. The reduced thermal expansion may be ascribed to the small TEC of SDC as well as the increased porosity due to the addition of SDC in the composite cathode, which will be further investigated from the microstructure of the materials. The curve of pure SCFN is nonlinear and the value of dL/L_0 increases upon heating first, and then shows an inflection range occurring at temperatures between 325 and 350 °C, which may be attributed to

the formation of oxide ion vacancies. And this conclusion is in excellent agreement with TGA analysis.

3.5. Microstructure

Fig. 9(a–f) shows the cross-sectional SEM micrographs of SCFN-xSDC layer sintered at 950 °C for 2 h on SDC electrolytes. The bottom of the micrograph indicates the dense, sintered SDC electrolyte, and the upper portion shows the porous cathode/composite electrodes. The SEM images indicate the good bonding and continuous contact at the interfaces, suggesting a good thermal compatibility between the electrolyte and cathode. The morphology of SCFN-xSDC powders are not a uniform mixture of fine particles. And the two oxides are separated completely from each other, but, more likely, an agglomerate mixture of the two components. The small SDC grains are dispersed homogeneously on the large SCFN particles surface and the interconnections

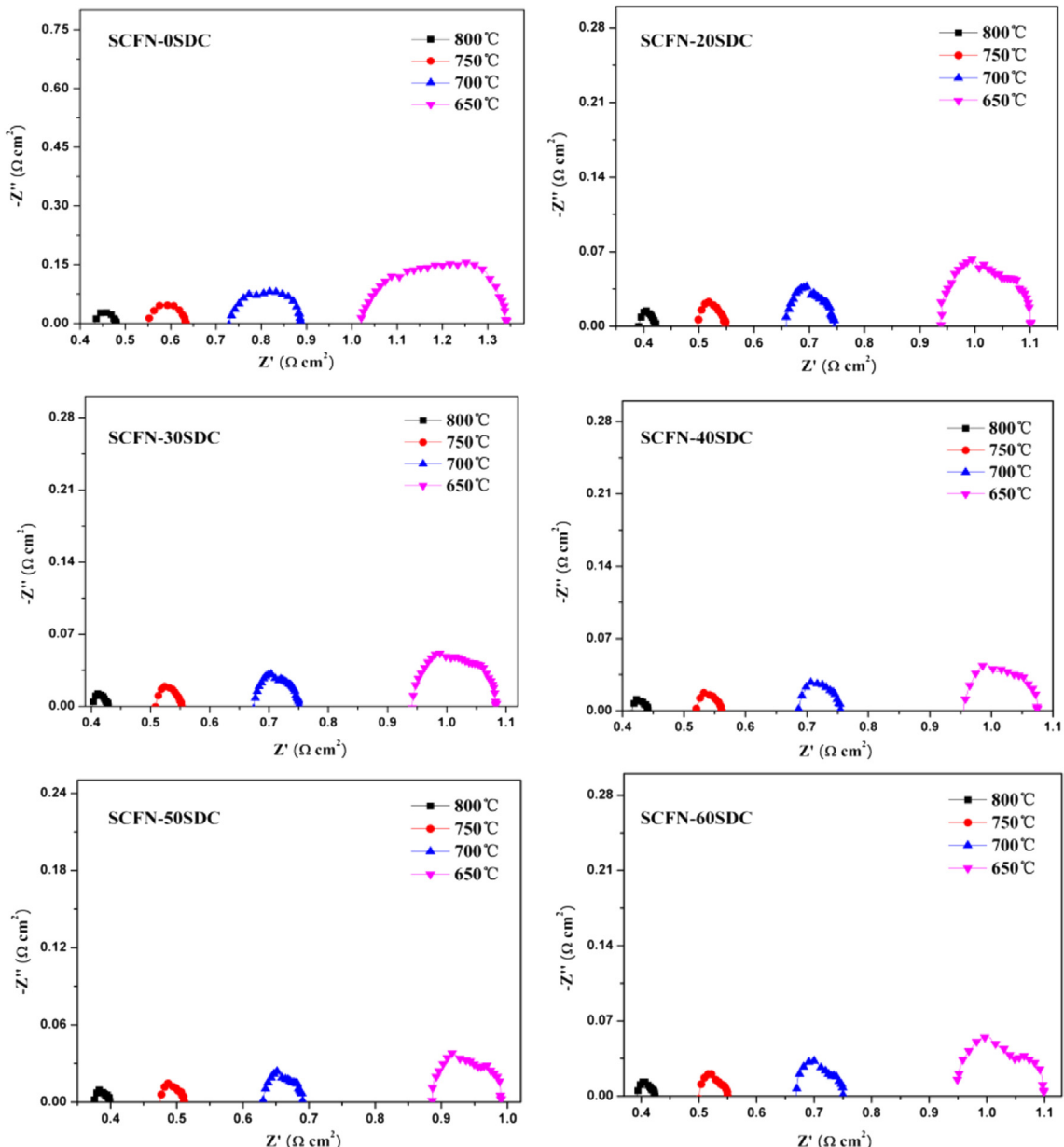


Fig. 11. Impedance spectra of SCFN-xSDC composite cathodes on SDC electrolyte measured at 650–800 °C in air.

between the two particles are much closer. Moreover, the cross-sectional image in Fig. 9(a–f) reveals a reasonable porosity to ensure gas diffusion. And the porosity of the SCFN–50SDC cathode is measured to be ~33.8% by image analysis. The composite cathodes provide high porosity, tortuosity and efficient current collection, and thus enlarge the electrochemically active areas via reducing the portion of the isolated catalysts, which is consistent with the low R_p values of these composites in Fig. 11. Fig. 9(g) shows the cross-sectional SEM image of NiO–SDC composite anode on SDC electrolyte sintered at 1250 °C for 4 h. The attachment of the composite anode is high and no delamination is observed at the NiO–SDC/SDC interface.

The surface microstructure and elemental composition of the SCFN–50SDC sample are characterized by SEM and EDS micro-analysis, which is shown in Fig. 10. The morphologies of the SCFN (irregular shape) and SDC (spherical shape) particles are distinguishable. The composite cathode consists of uniformly distributed nano-sized (100–200 nm) spherical SDC grains in the SCFN particles. In the examined cathode grain, only elements from the cathode can be detected. In the examined electrolyte grain, the higher apparent content of elements from the electrolyte can be detected, while some Sr, Co, Fe and Nb also appear due to the large area of excitation of the SEM beam of around 1.5 μm with the electrolyte.

3.6. Polarization resistance

In order to investigate the effect of SDC content on the performance of SCFN–xSDC composite cathodes, electrochemical impedance spectroscopy (EIS) of the symmetrical cells is investigated at different temperatures in air. Fig. 11 shows the EIS of SCFN–xSDC cathodes on SDC electrolyte measured at 650–800 °C in air. The right intercept on the real axis represents the total resistance (R_{tot}) and the left intercept on the real axis corresponds to the ohmic resistance (R_{ohm} , including the electrolyte, electrodes and connection wires). The polarization resistance (R_p) is estimated from the difference between R_{tot} and R_{ohm} ($R_p = R_{tot} - R_{ohm}$). From the impedance spectra, it can be seen that the R_p of SCFN–xSDC composite cathodes change from 0.0483 Ω cm² for pure SCFN to 0.0255 Ω cm² for SCFN–50SDC at 800 °C. The 47% decrease of R_p attributes to the large oxygen vacancy in SDC which is beneficial to establish sufficient TPBs and increase the paths to transfer the oxygen ions [43]. The detailed process can be explained as follows. As one kind of MIEC, SCFN with cubic perovskite structure, the oxygen reduction occurs not only on the TPBs but also on the surface of

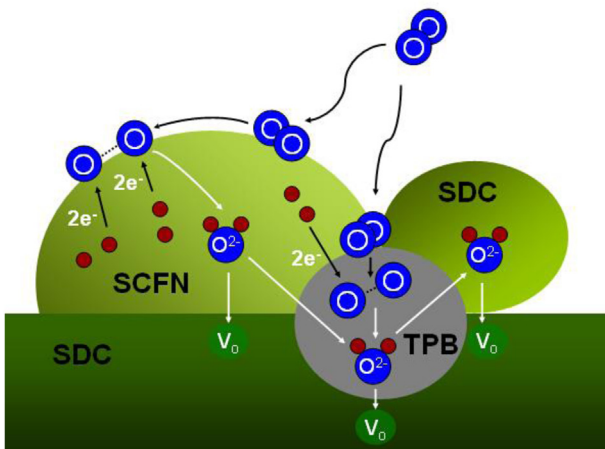


Fig. 12. Schematic of the possible process of oxygen reduction reaction in SCFN–xSDC composite cathodes.

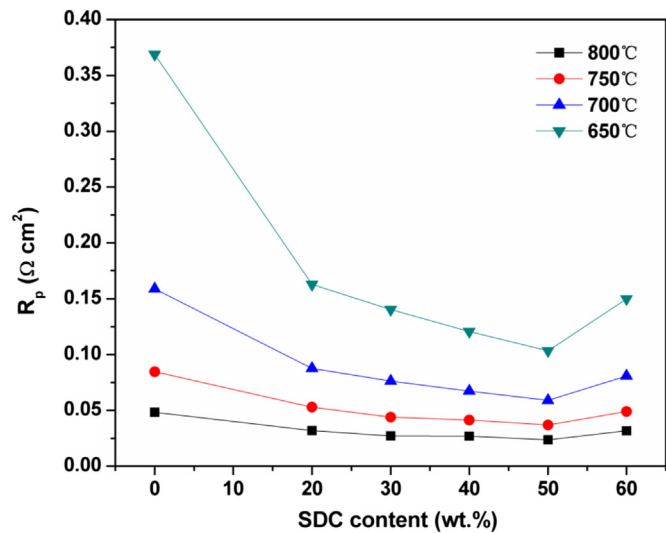


Fig. 13. Dependence of R_p for SCFN–xSDC composite cathodes with different SDC content at 650–800 °C in air.

cathode. The overall electrochemical reaction for oxygen reduction at a SOFC cathode can be simply described as an equation.



In reality, it may involve many sub-steps such as gas diffusion, surface adsorption, dissociation, electron and ion charge transfer, and so on [44]. In order to operate a cell in intermediate temperature range, it is of vital importance to accelerate the oxygen reduction reaction in the cathode and the oxygen transport in the cathode and electrolyte. Adler et al. [45,46] demonstrated that the oxygen reduction reaction in MIEC electrodes was governed by the oxygen surface exchange and the oxygen diffusion. The adsorbed molecular oxygen is first reduced to oxygen ions, and then diffuses toward the cathode–electrolyte interface and electrolyte bulk. Therefore, the oxygen vacancy is important for the oxygen reduction reaction in IT-SOFCs because they are closely related to oxygen

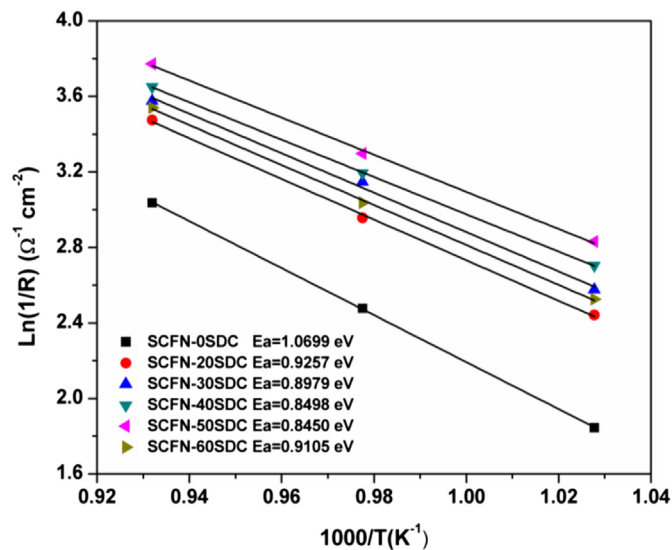


Fig. 14. Arrhenius plots of the polarization resistance of SCFN–xSDC cathode on SDC electrolyte.

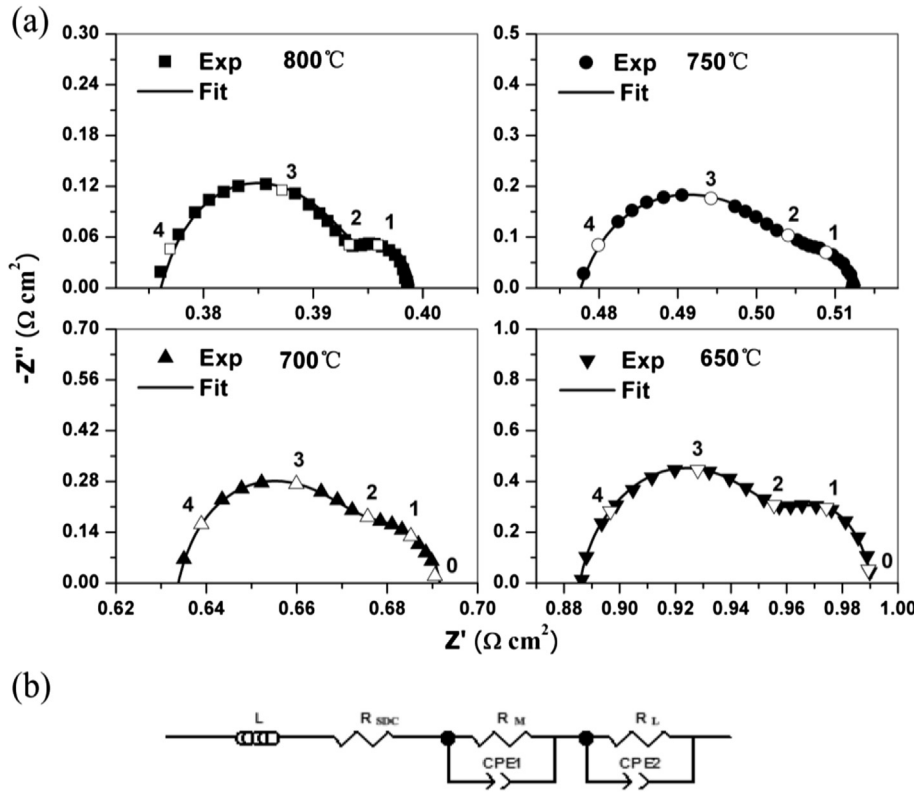


Fig. 15. (a) Experimental and fitting results of impedance spectra for the SCFN–50SDC/SDC/SCFN–50SDC symmetrical cell measured at various temperatures in air. The numbers in these plots correspond to logarithm of frequency; (b) the adopted equivalent circuit models.

dissociation, transportation, and incorporation. Moreover, the oxygen ions diffusion ability is limited by the concentration of oxygen vacancies [30]. Fig. 12 depicts the possible process of oxygen reduction reaction in SCFN–xSDC composite cathode on SDC electrolyte. The addition of SDC with proper content in the composite cathodes gives more channels to transport oxygen ions via increasing the concentration of total oxygen vacancies. Meanwhile, the TPBs increase when SDC is added into SCFN as a composite cathode. Hence, the oxygen reduction reaction can occur at much more TPBs, subsequently, more oxygen ions may diffuse to the SDC electrolyte, and the oxygen diffusion is improved.

The R_p values for the SCFN–xSDC composite cathodes at different temperatures are exhibited in Fig. 13. Increase of the SDC content from 0 to 50 wt% results in a continuous decrease in R_p , which indicates that SDC particles could accelerate the transport of oxygen ions through the electrode and results in better performance for the composite cathode. When the content of SDC in SCFN–xSDC cathode is 50 wt%, the lowest R_p is obtained at 800 °C. When SDC content increase from 50 to 60 wt%, the cathode polarization resistance increase, which presumably is caused by the decrease of electrochemical reaction sites with the decrease of SCFN. On the other hand, the electron transport channels of SCFN are blocked because of the reduced connectivity of SCFN with the increase of SDC content. EIS measurement results show that SCFN–50SDC cathode presents the lowest R_p in these composite cathodes at 650–800 °C. Similar results are reported in recent researches, for example, the addition of 50 wt% Ce_{0.9}Gd_{0.1}O_{1.95} (GDC) to SmBaCoFeO_{5+δ} cathode results in the reduced R_p compared with a cathode with 30 wt% GDC [47], and a mixture of 40 wt% SDC with Sr₂Fe_{1.5}Mn_{0.5}O₆ offers lower R_p [48]. And optimized R_p is reported in La_{0.6}Sr_{0.4}Co_{0.2}Fe_{0.8}O_{3-δ}: (60 wt%) GDC [49], SmBa_{0.5}Sr_{0.5}Co₂O_{5+δ}: (50 wt%) GDC [50] and La_{1-x}Sr_xMnO₃: (40 wt%) yttria-stabilized

zirconia (YSZ) [51]. Fig. 14 shows Arrhenius plots of the R_p values for SCFN–xSDC composite cathodes. The activation energy of the composite cathodes decreases compared to pure SCFN cathode because the addition of the SDC electrolyte effectively extends electrochemical TPBs and increases the number of active sites. A similar result has been reported in the SmBaCo₂O_{5+δ} and GDC composite cathodes, where the activation energies decrease with GDC content [52].

To get further knowledge of the electrochemical performance of SCFN–xSDC, the impedance spectra are fitted by the ZSimpWin software using the equivalent circuit models. As a typical example, Nyquist plots of the electrochemical impedance spectra for SCFN–50SDC cathode measured at various temperatures are shown in Fig. 15(a). The equivalent circuit for the analysis of the

Table 1

The fitting parameters for the impedance spectra (Fig. 15) of SCFN–50SDC/SDC/SCFN–50SDC symmetric cell measured at various temperatures in air.

T(°C)	800	750	700	650
Arc1	$L(H)$ 8.985×10^{-7}	8.021×10^{-7}	6.380×10^{-7}	3.585×10^{-7}
	$R(\Omega \text{ cm}^2)$ 0.367	0.467	0.622	0.870
	CPE_1-Q $(F \text{ cm}^{-2})$ 4.57×10^{-4}	4.30×10^{-4}	2.76×10^{-4}	2.74×10^{-4}
	CPE_1-n 0.62	0.59	0.61	0.60
	$R_1(\Omega \text{ cm}^2)$ 4.7×10^{-2}	6.9×10^{-2}	9.8×10^{-2}	1.68×10^{-1}
	$F_1(\text{Hz})$ 3239.1	2236.9	1747.7	1447.0
Arc2	$C_1(F \text{ cm}^{-2})$ 1.04×10^{-3}	1.03×10^{-3}	9.29×10^{-4}	6.55×10^{-4}
	CPE_2-Q $(F \text{ cm}^{-2})$ 2.74×10^{-2}	2.06×10^{-2}	9.06×10^{-3}	5.49×10^{-3}
	CPE_2-n 0.90	0.70	0.70	0.67
	$R_2(\Omega \text{ cm}^2)$ 8.0×10^{-3}	1.2×10^{-2}	3.0×10^{-2}	5.3×10^{-2}
	$F_2(\text{Hz})$ 9.03	12.62	21.00	23.00
	$C_2(F \text{ cm}^{-2})$ 2.20	1.05	0.25	0.13

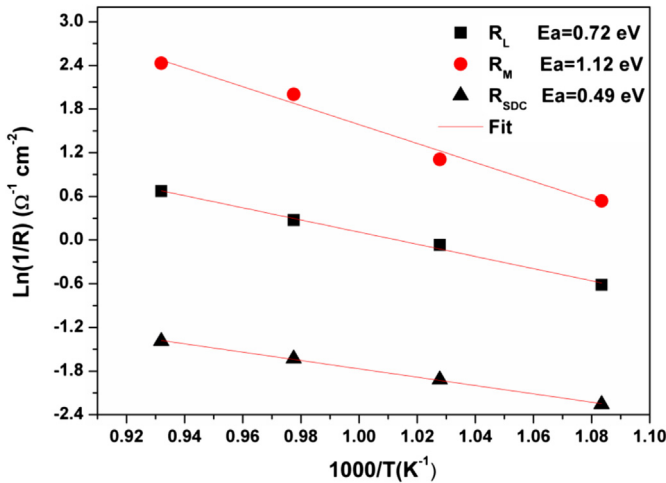


Fig. 16. Arrhenius plots of R_{SDC} , R_M and R_L of SCFN–50SDC cathode on SDC electrolyte.

impedance data is illustrated in Fig. 15(b). The R_{SDC} of the electrical equivalent circuit represents the electrolytic (SDC) resistance. L is the inductance originating from equipment and connection cables. R_M/CPE_1 and R_L/CPE_2 represent the resistance/capacitance due to middle and low frequency arcs, respectively. The impedances of a symmetric cell may arise from both the electrodes and electrolyte. As shown in Fig. 15(a), the electrolyte typically performs as an ideal resistor and displays only a dot in the Nyquist plots at different temperatures in the relatively high-frequency (HF). And two depressed semicircles are observed in the Nyquist plots. According to the impedance plots of MIEC reported by Adler [53], charge-transfer resistance originating from ion transfer at the interface of

electrode and electrolyte is observed for the mid-frequency (MF) arc, while the impedance at low-frequency (LF) is associated with non-charge transfer, such as oxygen surface exchange and gas-phase diffusion inside and outside the electrode layer. Table 1 summarizes the fitting parameters as a function of temperature for SCFN–50SDC electrode. The temperature dependence of the HF resistance (R_{SDC}), the MF resistance (R_M) and the LF resistance (R_L), is presented in Fig. 16. Evidently, the R_{SDC} , R_M and R_L exhibit Arrhenius behavior within the studied temperature range. The magnitude of the activation energy (E_a) 0.49 eV, which is obtained from temperature-dependent R_{SDC} , is slightly lower than the common reported values ($E_a \approx 0.77\text{--}1.03 \text{ eV}$) [54–56]. The slightly lower value for the estimated E_a is attributed to the nano-sized SDC particles. Therefore, assuming that R_{SDC} is the electrolyte resistance due to migration of O^{2-} through SDC electrolyte is justified. In addition, the decreased dependence of the R_M and R_L on the temperature (Fig. 16) agrees with previous reports [57]. To get more insight into the mechanism of oxygen reduction over the SCFN–50SDC electrode, the capacitance and angular relaxation frequency f , which is an independent parameter of sample geometric characteristics and is a very useful tool to identify the oxygen reduction process, are calculated based on the following equations [58]:

$$C_i = \frac{(R_i Q_i)^{\left(\frac{1}{n_i}\right)}}{R_i} \quad (4)$$

$$f_i = \frac{(R_i Q_i)^{-\left(\frac{1}{n_i}\right)}}{2\pi} \quad (5)$$

As shown in Table 1, both f and capacitance for MF arcs are similar to the reported values for oxide-ion transfer through the electrolyte–electrode interface [58]. Therefore, MF arc is assigned to the impedance associated with oxide-ion charge transfer through the

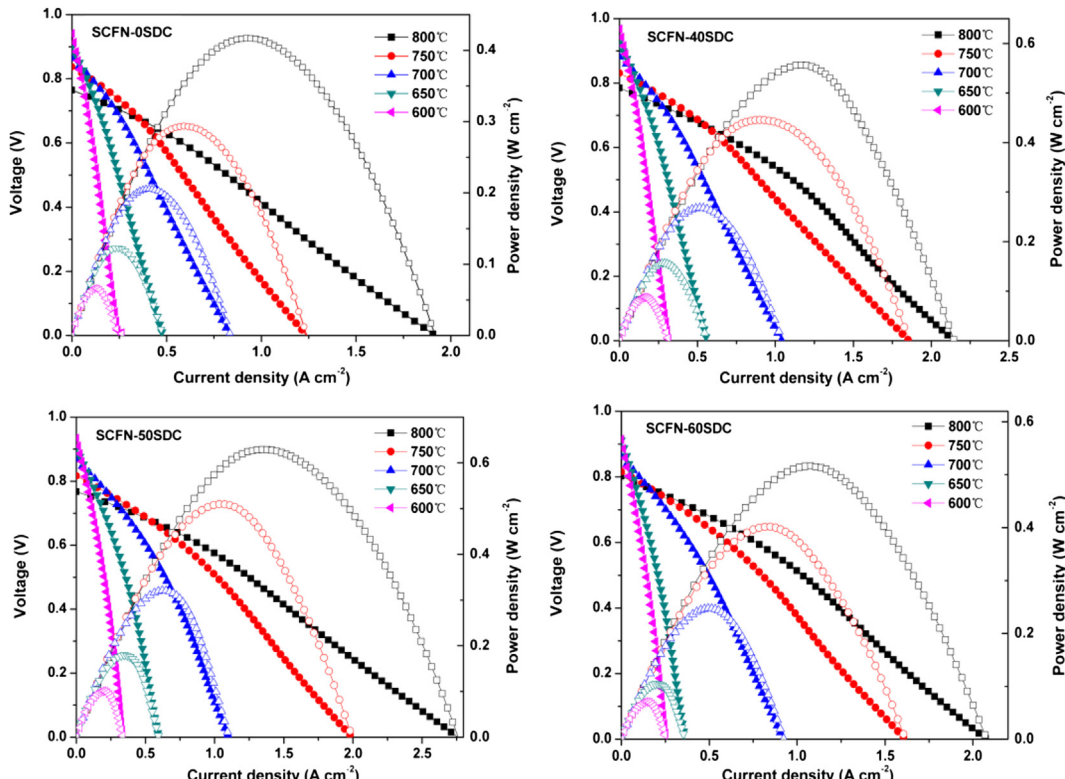


Fig. 17. Cell voltage and power density as functions of current density with SCFN–xSDC ($x = 0, 40, 50$ and 60) cathodes.

interface between SCFN–50SDC and SDC. The polarization resistance associated with this process is about 3/4–6/7 that of the total cathode oxygen reduction, suggesting the oxygen-ion charge transfer through the electrode–electrolyte plays an important role in the overall oxygen reduction in the SCFN–50SDC composite cathode.

3.7. Cell performance

Fig. 17(a)–(d) shows cell voltage and power density as a function of current density for the Ni–SDC/SDC/SCFN– x SDC cell with cathodes $x = 0, 40, 50$ and 60 , respectively. The cell is tested using dry H₂ as fuel and ambient air as oxidant in the temperature range of 600–800 °C. At 800 °C, the maximum power density values of the cell are 417, 557, 630 and 517 mW cm⁻² for SCFN– x SDC cathodes with $x = 0$ to 60 , respectively. This result is consistent with the R_p data mentioned above. High power densities demonstrate that SCFN– x SDC oxides are promising cathode materials for IT-SOFCs. In addition, the cell with SCFN–50SDC cathode presents a more excellent performance, compared to SCFN– x SDC cathode with $x = 0, 40$ and 60 . Therefore, the SCFN–50SDC cathode is preferred for applications in IT-SOFCs.

4. Conclusions

The SCFN oxide is investigated for the potential cathode for IT-SOFCs. The SCFN oxide has a pure cubic perovskite structure. The SCFN cathode material also shows a good chemical compatibility with the SDC electrolyte. There are no seriously reactions between SDC electrolyte and SCFN cathode except a slight peak shift. The XPS results indicate that the transition-metal cations in the SCFN oxide participate as mixed valence states of Co³⁺/Co⁴⁺, Fe³⁺/Fe⁴⁺, Nb⁴⁺/Nb⁵⁺. The conduction behavior of the SCFN oxide undergoes a change from semiconductor-like to metal-like around 350 °C. The addition of SDC lowers the TECs of SCFN sharply and reduces the thermal expansion mismatch. The SDC addition reduces the polarization resistance. The lowest R_p of 0.0255 Ω cm² is achieved at 800 °C for SCFN–50SDC composite cathode. When SCFN– x SDC is used as the cathode, the electrolyte-supported (thickness of electrolyte is 300 μm) single-cells get excellent performance. The maximum power density of cells for $x = 0, 40, 50$ and 60 are 417, 557, 630 and 517 mW cm⁻² at 800 °C, respectively. All results show that SCFN–50SDC composite cathode is a promising material for IT-SOFC based on SDC electrolytes, whose stability and performance on single cell will be investigated in the future.

Acknowledgments

The authors gratefully acknowledge the research funding provided by Program for the development of Science and Technology of Jilin province (Nos. 20140520103JH, 20140519003JH, 20120359, and 201201083), the Twentieth Five-Year Program for Science and Technology of Education Department of Jilin Province (No. 20130447), Program for the development of Science and Technology of Siping city (No. 2012036).

References

- [1] C. Zhu, X. Liu, D. Xu, D. Wang, D. Yan, L. Pei, T. Lü, W. Su, *J. Power Sources* 185 (2008) 212–216.
- [2] S.H. Jo, P. Muralidharan, D.K. Kim, *Electrochim. Commun.* 11 (2009) 2085–2088.
- [3] Z. Shao, S.M. Haile, *Nature* 431 (2004) 170–173.
- [4] A. Esquivel, N.P. Brandon, J.A. Kilner, M. Mogensen, *J. Electrochim. Soc.* 151 (2004) A1847–A1855.
- [5] Q. Ma, R. Peng, Y. Lin, J. Gao, G. Meng, *J. Power Sources* 161 (2006) 95–98.
- [6] T. Hibino, A. Hashimoto, M. Suzuki, *J. Electrochim. Soc.* 149 (2002) 1503–1508.
- [7] R. Peng, Y. Wu, L. Yang, Z. Mao, *Solid State Ionics* 177 (2006) 389–393.
- [8] V.V. Kharton, A.A. Yaremchenko, A.V. Kovalevsky, A.P. Viskup, E.N. Naumovich, P.F. Kerko, *J. Membr. Sci.* 163 (1999) 307–317.
- [9] K. Zhang, R. Ran, L. Ge, Z.P. Shao, W.Q. Jin, N.P. Xu, *J. Membr. Sci.* 323 (2008) 436–443.
- [10] P.Y. Zeng, Z.P. Shao, S.M. Liu, Z.P. Xu, *Sep. Purif. Technol.* 67 (2009) 304–311.
- [11] P.Y. Zeng, R. Ran, Z.H. Chen, W. Zhou, H.X. Gu, Z.P. Shao, S.M. Liu, *J. Alloys Compd.* 455 (2008) 465–470.
- [12] Y.P. Li, E.R. Maxey, J.W. Richardson, *J. Am. Ceram. Soc.* 88 (2005) 1244–1252.
- [13] A. Aguadero, D. Pérez-Coll, C. de la Calle, J.A. Alonso, M.J. Escudero, L. Daza, *J. Power Sources* 192 (2009) 132–137.
- [14] B. Lin, S.L. Wang, H.L. Liu, K. Xie, H.P. Ding, M.F. Liu, G.Y. Meng, *J. Alloys Compd.* 472 (2009) 556–558.
- [15] V.V. Vashook, M.V. Zinkevich, H. Ullmann, J. Paulsen, N. Trofimienko, K. Teske, *Solid State Ionics* 99 (1997) 23–32.
- [16] Z.Q. Deng, W.S. Yang, W. Liu, C.S. Chen, *J. Solid State Chem.* 179 (2006) 362–369.
- [17] W. Zajac, K. Świerczek, J. Molenda, *J. Power Sources* 173 (2007) 675–680.
- [18] C.R. Dyck, Z.B. Yu, V.D. Krstic, *Solid State Ionics* 171 (2004) 17–23.
- [19] K.T. Lee, A. Manthiram, *Solid State Ionics* 176 (2005) 1521–1527.
- [20] S. McIntosh, Jaap F. Vente, W.G. Haije, Dave H.A. Blank, J.M. Henny, *Solid State Ionics* 177 (2006) 1737–1742.
- [21] L.M. Liu, T.H. Lee, L. Qiu, Y.L. Yang, A.J. Jacobson, *Mater. Res. Bull.* 31 (1996) 29–35.
- [22] T. Nagai, W. Ito, T. Sakon, *Solid State Ionics* 177 (2007) 3433–3444.
- [23] O. Yu Podyacheva, Z.R. Ismagilov, A.N. Shmakov, M.G. Ivanov, A.N. Nadeev, S.V. Tsybulya, V.A. Rogov, *Catal. Today* 147 (2009) 270–274.
- [24] V. Dusastre, J.A. Kilner, *Solid State Ionics* 126 (1999) 163–174.
- [25] H. Gu, H. Chen, L. Gao, L. Guo, *Electrochim. Acta* 54 (2009) 7094–7098.
- [26] S.J. Lee, P. Muralidharan, S.H. Jo, D.K. Kim, *Electrochim. Commun.* 12 (2010) 808–811.
- [27] L. Cong, T. He, Y. Ji, P. Guan, Y. Huang, W. Su, *J. Alloys Compd.* 348 (2003) 325–331.
- [28] H.Y. Tu, Y. Takeda, N. Imanishi, O. Yamamoto, *Solid State Ionics* 100 (1997) 283–288.
- [29] S.Y. Li, Z. Lü, B. Wei, X.Q. Huang, J.P. Miao, G. Cao, W.H. Su, *J. Alloys Compd.* 426 (2006) 408–414.
- [30] S.Y. Li, Z. Lü, B. Wei, X.Q. Huang, J.P. Miao, Z.G. Liu, W.H. Su, *J. Alloys Compd.* 448 (2008) 116–121.
- [31] H. Falcón, J.A. Barbero, G. Araujo, M.T. Casais, M.J. Martínez-Lope, J.A. Alonso, J.L.G. Fierro, *Appl. Catal. B Environ.* 53 (2004) 37–45.
- [32] J.C. Dupina, D. Gonbeau, H. Benqlilou-Moudden, Ph. Vinatier, A. Levasseur, *Thin Solid Films* 384 (2001) 23–32.
- [33] E. Meza, J. Ortiz, D. Ruiz-León, J.F. Marco, J.L. Gautier, *Mater. Lett.* 70 (2012) 189–192.
- [34] M. O'Connell, A.K. Norman, C.F. Huettermann, M.A. Morris, *Catal. Today* 47 (1999) 123–132.
- [35] J. Jung, D.D. Edwards, *J. Solid State Chem.* 184 (2011) 2238–2243.
- [36] Prabhakar Singh, Benjamin J. Brandenburg, C. Peter Sebastian, Devendra Kumar, *Mater. Res. Bull.* 43 (2008) 2078–2084.
- [37] F. Wang, Q.J. Zhou, T.M. He, G.D. Li, H. Ding, *J. Power Sources* 195 (2010) 3772–3778.
- [38] B. Wei, Z. Lü, S. Li, Y. Liu, K. Liu, W. Su, *Electrochim. Solid State Lett.* 8 (2005) A428–A431.
- [39] J.W. Stevenson, T.R. Armstrong, R.D. Carneim, L.R. Pederson, W.J. Weber, *J. Electrochim. Soc.* 143 (1996) 2722–2729.
- [40] H. Zhao, W. Shen, Z. Zhu, X. Li, Z. Wang, *J. Power Sources* 182 (2008) 503–509.
- [41] S.Q. Lü, Y. Ji, X.W. Meng, G.H. Long, T. Wei, Y.L. Zhang, T.Q. Lü, *Electrochim. Solid State Lett.* 12 (6) (2009) B103–B105.
- [42] T.Z. Jiang, Z.H. Wang, B.Y. Ren, J.S. Qiao, W. Sun, K.N. Sun, *J. Power Sources* 247 (2014) 858–864.
- [43] J. Zhou, G. Chen, K. Wu, Y.H. Cheng, *J. Power Sources* 232 (2013) 332–337.
- [44] D.J. Chen, R. Ran, K. Zhang, J. Wang, Z.P. Shao, *J. Power Sources* 188 (2009) 96–105.
- [45] S.B. Adler, *Solid State Ionics* 111 (1998) 125–134.
- [46] S.B. Adler, J.A. Lane, B.C.H. Steele, *J. Electrochim. Soc.* 143 (1996) 35–54.
- [47] S.Q. Lü, G.H. Long, Y. Ji, X.W. Meng, C.C. Sun, *Int. J. Hydrogen Energy* 35 (2010) 7930–7935.
- [48] N.N. Dai, Z.L. Lou, Z.H. Wang, X.X. Liu, Y.M. Yan, J.S. Qiao, T.Z. Jiang, K.N. Sun, *J. Power Sources* 243 (2013) 766–772.
- [49] Y.J. Leng, S.H. Chan, Q. Liu, *Int. J. Hydrogen Energy* 33 (2008) 3808–3817.
- [50] J.H. Kim, M. Cassidy, John T.S. Irvine, J. Bae, *J. Electrochim. Soc.* 156 (6) (2009) B682–B689.
- [51] J.D. Kim, G.D. Kim, J.W. Moon, Y. Park, W.H. Lee, K. Kobayashi, M. Nagai, C.E. Kim, *Solid State Ionics* 143 (2001) 379–389.
- [52] J.H. Kim, Y. Kim, Paul A. Connor, John T.S. Irvine, J. Bae, W.Z. Zhou, *J. Power Sources* 194 (2009) 704–711.
- [53] S.B. Adler, *Solid State Ionics* 135 (2000) 603–612.
- [54] B.C.H. Steele, *Solid State Ionics* 129 (2000) 95–110.
- [55] Z.L. Zhan, T.L. Wen, H.Y. Tu, Z.Y. Lu, *J. Electrochim. Soc.* 148 (2001) A427–A432.
- [56] V. Esposito, E. Traversa, *J. Am. Ceram. Soc.* 91 (2008) 1037–1051.
- [57] P. Hjalmarsson, M. Mogensen, *J. Power Sources* 196 (2011) 7237–7244.
- [58] M.J. Escudero, A. Aguadero, J.A. Alonso, L. Daza, *J. Electroanal. Chem.* 611 (2007) 107–116.